Received: 31 August 2024 | Revised: 20 November 2024 | Accepted: 11 December 2024

DOI: 10.1002/inf2.12656

RESEARCH ARTICLE

WILEY

Simultaneous passivation of surface and bulk defects in all-perovskite tandem solar cells using bifunctional lithium salts

Yeonghun Yun[1,2] | Devthade Vidyasagar[1] | Sunwoo Kim[1] | Sung Woong Yang[1] | Doyun Im[1] | Rajendra Kumar Gunasekaran[1] | Sangheon Lee[3] | Jina Jung[1] | Won Chang Choi[1] | Roy Byung Kyu Chung[1] | Dong Hoe Kim[3] | Ji-Sang Park[4] | Sangwook Lee[1]

[1]School of Materials Science and Engineering, Kyungpook National University, Daegu, Republic of Korea

[2]Department Perovskite Tandem Solar Cells, Helmholtz-Zentrum Berlin für Materialien und Energie GmbH, Berlin, Germany

[3]Department of Materials Science and Engineering, Korea University, Seoul, Republic of Korea

[4]SKKU Advanced Institute of Nano Technology, Sungkyunkwan University, Suwon, Republic of Korea

Correspondence

Sangwook Lee, School of Materials Science and Engineering, Kyungpook National University, Daegu 41566, Republic of Korea.
Email: wook2@knu.ac.kr

Dong Hoe Kim, Department of Materials Science and Engineering, Korea University, Seoul 02841, Republic of Korea.
Email: donghoekim@korea.ac.kr

Ji-Sang Park, SKKU Advanced Institute of Nano Technology, Sungkyunkwan University, Suwon 16419, Republic of Korea.
Email: jisangpark@skku.edu

Funding information

National Research Foundation of Korea, Grant/Award Numbers: 2022M3J1A1085285, RS-2023-00302646, 2022M3H4A1A03074093

Abstract

All-perovskite tandem solar cells have garnered considerable attention because of their potential to outperform single-junction cells. However, charge recombination losses within narrow-bandgap (NBG) perovskite subcells hamper the advancement of this technology. Herein, we introduce a lithium salt, lithium bis(trifluoromethanesulfonyl)imide (LiTFSI), for modifying NBG perovskites. Interestingly, LiTFSI bifunctionally passivates the surface and bulk of NBG by dissociating into Li^+ and $TFSI^-$ ions. We found that $TFSI^-$ passivates halide vacancies on the perovskite surface, reducing nonradiative recombination, while Li^+ acts as an interstitial n-type dopant, mitigating the defects of NBG perovskites and potentially suppressing halide migration. Furthermore, the underlying mechanism of LiTFSI passivation was investigated through the density functional theory calculations. Accordingly, LiTFSI facilitates charge extraction and extends the charge carrier lifetime, resulting in an NBG device with power conversion efficiency (PCE) of 22.04% (certified PCE of 21.42%) and an exceptional fill factor of 81.92%. This enables the fabrication of all-perovskite tandem solar cells with PCEs of 27.47% and 26.27% for aperture areas of 0.0935 and 1.02 cm^2, respectively.

KEYWORDS

all-perovskite tandem solar cells, defect passivation, LiTFSI salt, narrow-bandgap perovskites, nonradiative charge recombination

1 | INTRODUCTION

All-perovskite tandem solar cells are constructed using a combination of mixed-Sn/Pb narrow-bandgap (NBG; ~1.2 eV) perovskite subcells and mixed I/Br wide-bandgap (WBG; ~1.8 eV) perovskite subcells.[1–5] These tandems have garnered significant attention recently due to their potential to achieve power conversion efficiencies (PCEs) exceeding 40%, stemming from their extended absorption spectra and reduced thermal losses.[6] Consequently, their PCE has rapidly improved over the past few years, with a certified PCE of 29.1% surpassing that of single-junction solar cells.[7,8] Beyond their high efficiency, owing to their versatility, including flexibility and suitability for application in space, all-perovskite tandem solar cells are considered the next generation of photovoltaics (PVs).[9,10]

Advancements in NBG perovskite solar cells (PSCs) have been pivotal in driving progress in all-perovskite tandem technology.[2,11,12] For instance, Zhao et al. achieved a PCE of 21.0% in all-perovskite tandems by enhancing NBG perovskite quality through chlorine incorporation.[13] Lin et al. significantly improved the PCE to 24.8% by introducing metallic Sn into the precursor solution to suppress Sn^{2+} oxidation.[2] Furthermore, Lin et al. enhanced NBG perovskite subcells with a 3D/3D bilayer, resulting in a PCE exceeding 28.0%.[7] Numerous strategies have been explored to optimize NBG perovskites further, including controlling lattice strain and defects at grain boundaries in the NBG film bulk,[14–16] and mitigating iodine vacancies and compositional inhomogeneity at the NBG surface.[17–19] Among these strategies, perovskite/perovskite heterojunctions, particularly 2D/3D perovskite structures, have gained recognition because of their effectiveness in passivating surface defects and inhibiting oxidation.[20–24] In particular, bulky organic cations bound with iodine, such as phenethylammonium, butylammonium, and 4-amidinopyridine as well as possibly ethylenediammonium, and propane-1,-3-diammonium are excellent agents for 2D perovskite upper layer.[18,20,21,25]

Despite the advantages of 2D perovskite layers, persistent surface charge carrier losses remain challenging to overcome and cannot be easily addressed by introducing additional 2D layers. This difficulty arises from the low out-of-plane conductivity and uneven potential distribution in 2D perovskite layers.[7] Moreover, the usage of halide-based materials for further surface treatment is hindered by the low activation energy of halide migration, leading to changes in stoichiometry and material properties.[26,27]

From this perspective, lithium bis(trifluoromethanesulfonyl) imide (LiTFSI) is anticipated to be beneficial for NBG perovskite passivation. The LiTFSI is expected to effectively address positively and negatively charged defects without introducing detrimental effects such as increased series resistance. Li^+ ions, owing to their small size (70 pm), can compensate for cation defects at the surface and grain boundaries without forming a resistive 2D perovskite layer. Simultaneously, $TFSI^-$ ions can efficiently compensate surface I^- vacancies—common defects in perovskite materials. In addition, LiTFSI is anticipated to prevent the surface oxidation of NBG perovskites by interacting with Pb-terminated and methylammonium (MA^+)-terminated planes through strong coordination with unbound A-site (MA^+, formamidinium; FA^+, and Cs^+) and B-site (Pb^{2+} and Sn^{2+}) cations. While LiTFSI has been widely used as a dopant for 2,2′,7,7′-Tetrakis[*N*,*N*-di(4-methoxyphenyl)amino]-9,9′-spirobifluorene (Spiro-OMeTAD), a hole transporting material in n-i-p structured PSCs, its potential as a defect passivant for NBG perovskites remains unexplored.[28–30]

Herein, we used LiTFSI to alleviate surface charge carrier losses and improve the environmental stability of an NBG perovskite. Remarkably, LiTFSI exhibited a bifunctional impact on both the surface and bulk of NBG perovskite, with $TFSI^-$ and Li^+ ions distributed at the surface and the entire NBG perovskite, respectively. This facilitated charge extraction at the NBG perovskite surface and extended the charge carrier lifetime, allowing to achieve an impressive PCE of 22.04% (certified PCE of 21.42%) in a single-junction NBG PSC, with a remarkable fill factor (FF) of 81.92% and an open-circuit voltage (V_{OC}) of 0.832 V. The improved FF and V_{OC} of NBG subcell subsequently resulted in high PCEs of all-perovskite tandem solar cells, exhibiting PCEs of 27.47% and 26.27% for aperture areas of 0.0935 and 1.02 cm^2, respectively. Furthermore, these tandem structures maintained over 80% of the initial PCE after 240 h of continuous operation.

2 | RESULTS AND DISCUSSION

2.1 | LiTFSI for single-junction NBG PSCs

To evaluate the effectiveness of LiTFSI, we constructed NBG PSCs with a p-i-n architecture of glass/fluorine-doped tin oxide (FTO)/poly(3,4-ethylenedioxythiophene) polystyrene sulfonate (PEDOT:PSS)/NBG perovskite/C_{60}/bathocuproine (BCP)/Cu. Figure 1A compares the PV parameters of control and LiTFSI-treated devices. Detailed statistical values are presented in Table 1. Evidently, the introduction of LiTFSI increases FF and V_{OC} while having minimal effect on short-circuit current density (J_{SC}). This trend is consistently reflected in

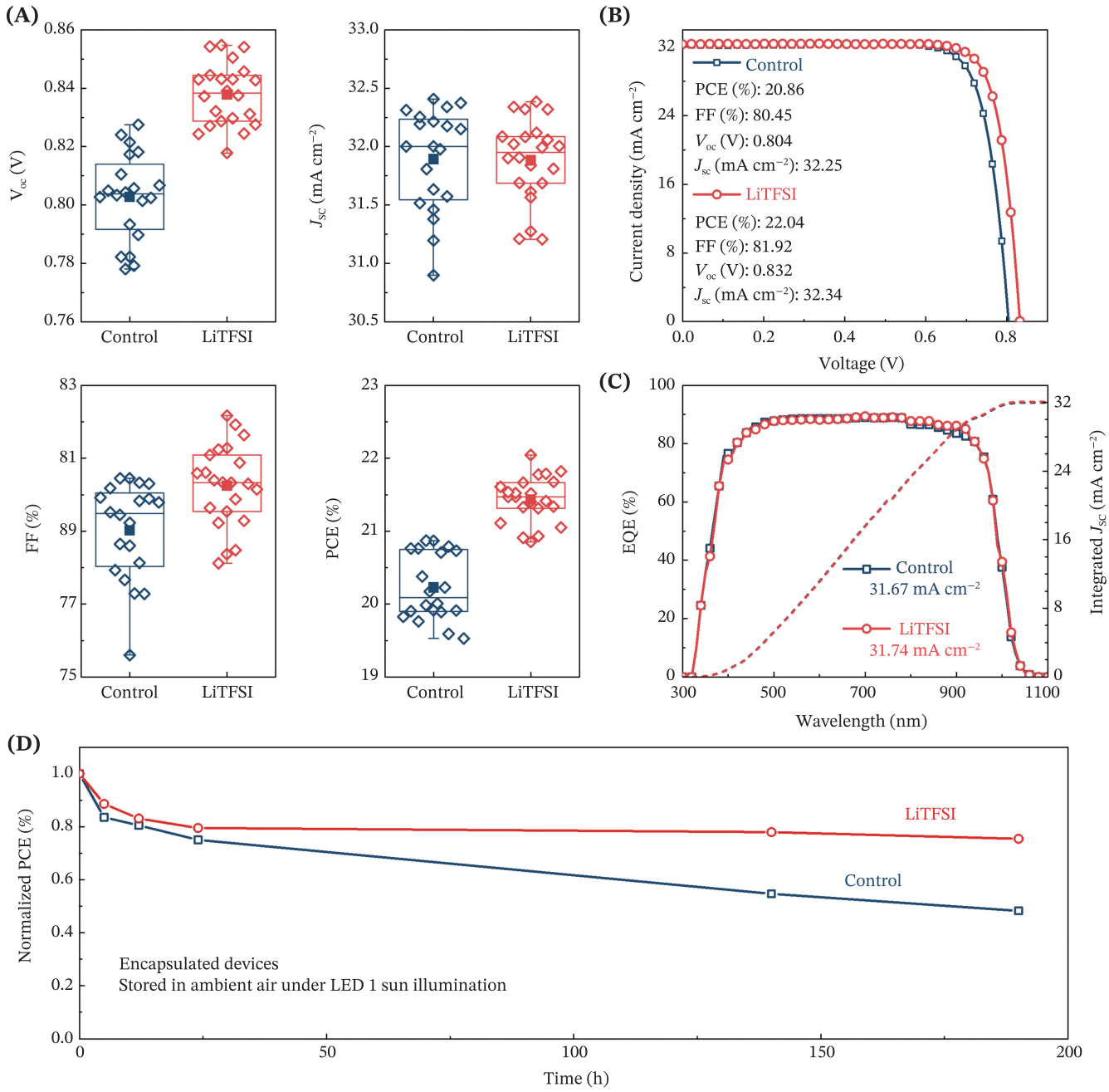

FIGURE 1 Effect of LiTFSI on single-junction NBG PSCs. (A) Statistical box plots for PV parameters of control and LiTFSI-treated NBG PSCs (V_{OC}, J_{SC}, FF, and PCE). (B, C) *J–V* curves (B) and EQE spectra with integrated J_{SC} (C) of the best-performing devices. (D) Long-term PCE-tracking results for encapsulated NBG devices. Devices were maintained under continuous 1 sun illumination in ambient air at a relative humidity of 30%–50%. Forced cooling of the devices was not performed during storage and measurement, and environmental temperature was maintained at ~22°C. The initial PCEs of control and LiTFSI-treated single-junction NBG PSCs were 19.85% (V_{OC} = 0.828 V, FF = 75.22%, and J_{SC} = 31.87 mA cm^{-2}) and 21.79% (V_{OC} = 0.846 V, FF = 80.88%, and J_{SC} = 31.84 mA cm^{-2}), respectively.

current density–voltage (*J–V*) curves of the best-performing devices (Figure 1B). The best-performing LiTFSI-treated solar cell exhibits a higher PCE (22.04%) than the control device (20.86%), as well as higher FF (81.92% vs. 80.45%) and V_{OC} (0.832 vs. 0.804 V). The steady-state PCEs of the control and LiTFSI-treated devices are 20.4% and 21.5%, respectively (Figure S1). The certified PCE of the LiTFSI-treated device is 21.42%, which is in good agreement with the in-lab value (Figure S2). The J_{SC} value calculated from external quantum efficiency (EQE) is consistent with the value obtained through the *J–V*

TABLE 1 PV parameters of single-junction control and LiTFSI-treated NBG PSCs.

	J_{SC} (mA cm^{-2})	V_{OC} (V)	FF (%)	PCE (%)
Control				
Average	31.90 ± 0.43	0.803 ± 0.015	79.02 ± 1.30	20.23 ± 0.45
Best	32.25	0.804	80.45	20.86
LiTFSI				
Average	31.88 ± 0.34	0.838 ± 0.010	80.25 ± 1.09	21.43 ± 0.31
Best	32.34	0.832	81.92	22.04

measurements (Figure 1C). LiTFSI treatment did not change the film thickness and bandgap (Figures S3 and S4).

Subsequently, we monitored the stability of the devices, as shown in Figure 1D. The encapsulated devices were exposed to ambient air under continuous 1 sun illumination without additional cooling at ~22°C. Both control and LiTFSI-treated devices exhibited distinct two PCE loss regimes: a fast initial PCE loss (burn-in) regime and a relatively slow PCE loss regime. Notably, this burn-in stage in NBG PSCs has been documented in previous studies.[12,31] Furthermore, it is known to be a temporary and reversible loss, typically recoverable if the devices are stored in dark conditions for a certain period.[32–34] While the exact cause of the initial burn-in remains unclear, we attribute it to the characteristics of NBG subcells, as evidenced by the absence of a similar burn-in stage in the MPP tracking results of tandem devices (this will be discussed later), where the NBG perovskite absorbs only half of its potential absorption spectrum (Figure 4F). The LiTFSI-based device exhibits considerably higher stability, retaining ~78% of its initial PCE after 140 h, whereas the control device loses ~45% of its initial PCE within the same period. Given that the relatively slow PCE reduction regime is attributed to irreversible losses such as chemical reactions and defects,[32,34] we attribute the improved stability of LiTFSI-treated devices to the suppression of defects and inhibition of oxidation, topics which will be elaborated on in subsequent sections.

2.2 | Charge carrier dynamics and PCE loss mechanism

To gain insights into the enhancement of PV performance with LiTFSI, we analyzed the charge carrier dynamics. We used steady-state photoluminescence (PL) to investigate charge recombination in NBG films deposited on glass substrates (Figure 2A). The PL peaks for the NBG films are observed at 1010 nm, indicating that LiTFSI did not considerably affect the bandgap, as shown earlier (Figure S4). However, PL intensity markedly increases with the incorporation of LiTFSI, suggesting a reduction in nonradiative recombination. The suppression of nonradiative recombination was further confirmed using glass/PEDOT:PSS/NBG perovskite/C_{60} in time-resolved PL (TRPL) measurements (Figure 2B). The TRPL decay fitted using a triexponential model (Table S1) revealed that effective lifetime (τ_{eff}) in LiTFSI-treated NBG (112.1 ns) is more than two times longer than that in the control sample (54.2 ns). Confocal fluorescence lifetime images further highlight a clear difference in the lifetime and its homogeneity over the entire measured area (20 × 20 μm^2; Figure 2C). Furthermore, we calculated the differential lifetimes based on TRPL results to better understand charge carrier recombination at the interface (Figure 2D). The higher plateau for the LiTFSI-treated NBG than for the control NBG indicates that LiTFSI effectively reduces recombination at the interface.[35,36]

To quantitatively assess the effect of LiTFSI on NBG defect passivation, trap density was determined from the space charge–limited current by characterizing dark current–voltage (*I*–*V*) curves (Figures 2E and S5). The devices with LiTFSI exhibit considerably lower electron and hole trap densities than the control devices. These improvements were attributed to the ionic nature of LiTFSI, which can effectively passivate positive and negative defects. In addition, we assessed the built-in potential (V_{bi}) difference by performing Mott–Schottky analyses (Figure 2F). The NBG device with LiTFSI shows a V_{bi} of 0.778 V, whereas the device without LiTFSI exhibits V_{bi} of 0.740 V. The high V_{bi} of the device with LiTFSI implies energetic alignment changes and suggests that reduced surface trap density and improved interfacial charge transport contribute to enhanced PV performance.[11]

To further elucidate the mechanism behind PCE losses, we extracted the ideality factor (n_{id}) from the slope of light intensity–dependent V_{OC} measurements (Figure S6). The n_{id} value reflects the extent of V_{OC} loss primarily caused by trap-induced nonradiative recombination.[37–39] The n_{id} value of the LiTFSI sample is 1.17, whereas that of the control is 1.25, suggesting a reduction in trap-induced recombination under open-circuit conditions. Next, we reconstructed the pseudo-*J*–*V* (p*J*–*V*) curves to understand the increase in FF caused by LiTFSI (Figure 2G, see the following explanation in Figure S6). p*J*–*V* curves limited only by nonradiative recombination in the devices were obtained using light intensity–dependent V_{OC}.[40,41] When comparing the pFF with the Shockley–Queisser limit, the incorporation of LiTFSI reduced nonradiative (2.42% absolute) and charge transport (3.78% absolute) losses

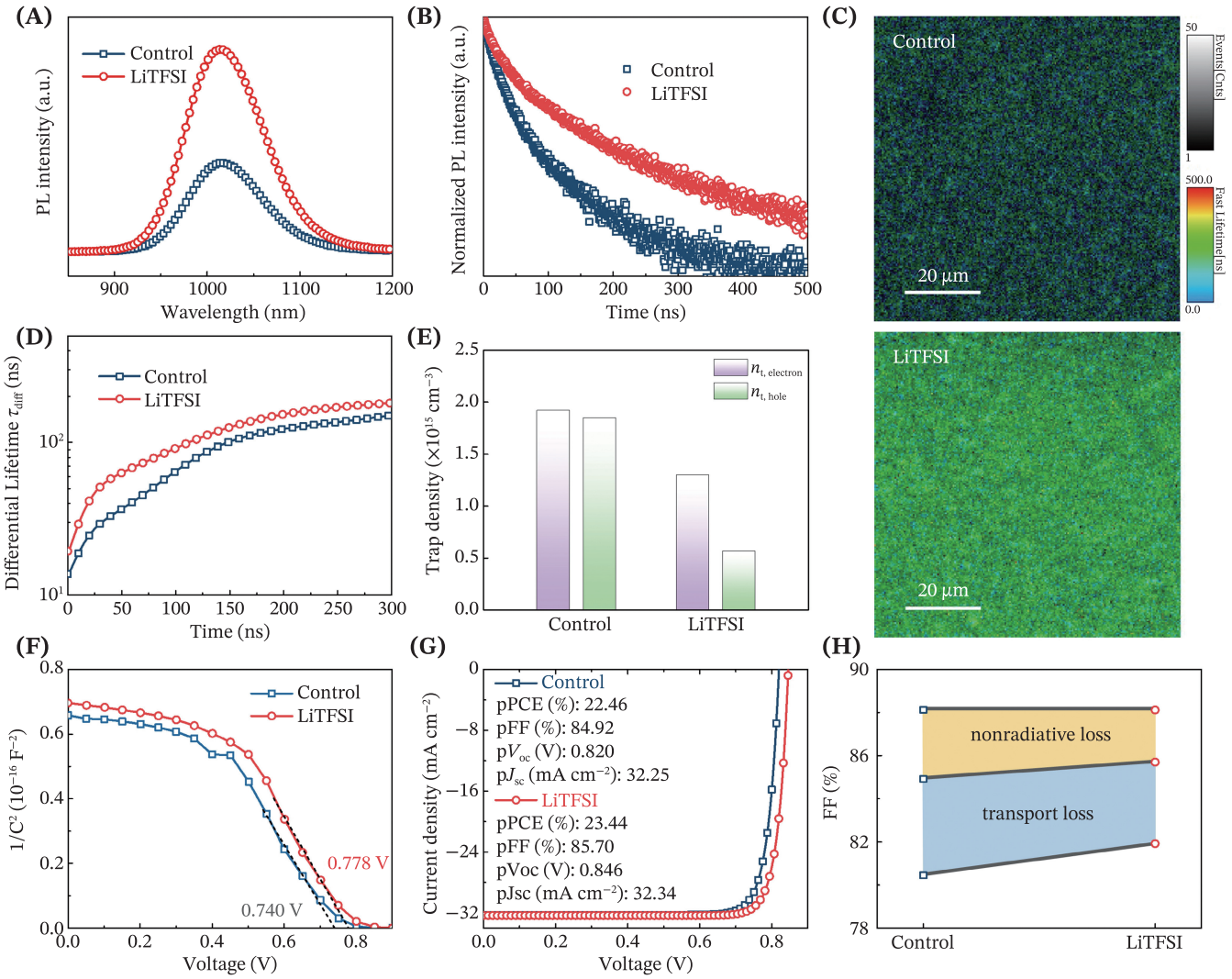

FIGURE 2 Analyses of charge carrier dynamics and PCE loss mechanism. (A) Steady-state PL spectra of NBG films with and without LiTFSI. The configuration of the films used for steady-state PL measurements is glass/NBG perovskite. (B) TRPL spectra of the NBG films containing FTO/PEDOT:PSS/NBG perovskite/C_{60}. (C) Confocal fluorescence lifetime images of control and LiTFSI-treated NBG films. (D) Computed differential lifetimes of the NBG films. The differential lifetimes were obtained considering the derivatives of exponential fits shown in Figure 2B. (E) Electron and hole trap densities of control and LiTFSI-treated NBG devices were obtained from the characterization of dark *I–V* curves (Figure S5). (F) Mott–Schottky curves of control and LiTFSI-treated PSCs. (G) p*J–V* curves of the control and LiTFSI-treated NBG PSCs reconstructed from the intensity-dependent V_{OC} measurements (Figure S6). (H) Schematic of FF loss mechanism under each condition. The specific values are presented in Figure 2G and Table S2.

compared with the control, which exhibits nonradiative loss of 3.20% absolute and charge transport loss of 4.47% absolute (Figure 2H). This indicates that LiTFSI not only suppressed nonradiative recombination but also promoted charge transport, probably through defect passivation within the bulk and at the surface. These improvements contribute to enhanced FF in LiTFSI-treated devices. Moreover, the empirically obtained FF values agree well with those obtained from the p*J–V* curves, thereby confirming the reduction in FF loss (Table S2).

2.3 | Characterization of LiTFSI-treated NBG perovskite film

To further elucidate the effects of LiTFSI on NBG perovskites, we investigated the thin-film properties of the LiTFSI-treated perovskite. Time-of-flight secondary ion mass spectrometry (ToF-SIMS) was used to determine the distribution of LiTFSI in the perovskite, as shown in Figures 3A and S7. As expected, $TFSI^-$ ions are predominantly observed at the film surface because of their larger

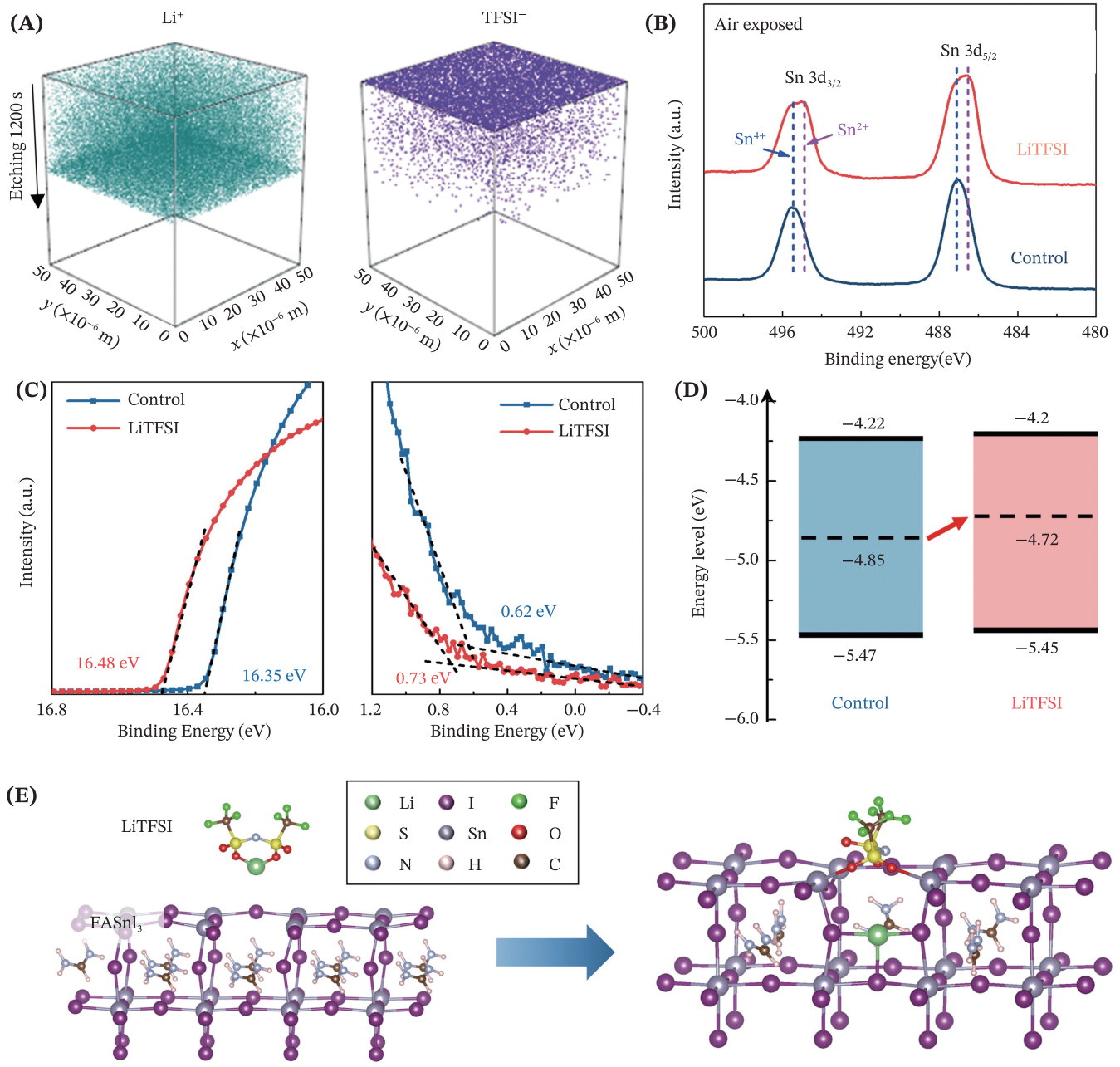

FIGURE 3 Characterization of NBG perovskite films and an overview of LiTFSI treatment strategy. (A) 3D maps showing the distributions of Li^+ and $TFSI^-$ ions within LiTFSI-treated NBG perovskite film. (B) XPS spectra of Sn $3d_{3/2}$ and $3d_{5/2}$ core levels for the control and LiTFSI-treated NBG films. Films were exposed to ambient air at a relative humidity of 30%–50% for 12 h. (C) Spectra of the NBG films with and without LiTFSI. (D) Schematic of energetic levels derived from the UPS spectra. (E) DFT calculation results investigating the reaction mechanism of LiTFSI treatment.

size (899 pm) compared with I^- (220 pm) and high activation energy of ion migration.[42] At the same time, Li^+ ions are distributed throughout the NBG perovskite film because small Li^+ ions (70 pm) can diffuse relatively easily into the perovskite bulk. The diffusion of Li^+ ions into the bulk perovskite and the associated benefits of Li^+ incorporation, including the introduction of n-type doping, suppression of halide migration, passivation of grain boundaries and bulk defects, and improved charge carrier dynamics, have been previously reported.[43–47] By contrast, no significant signal of $TFSI^-$ and Li^+ is detected for the control NBG perovskite film.

We also performed x-ray photoelectron spectroscopy (XPS) to investigate the changes in the chemical state of the perovskite film after incorporating LiTFSI. The interaction between LiTFSI and the perovskite film is discerned through a shift in the binding energy of metal cation and halide, as depicted in Figure S8. The shift in

peak positions for Sn^{2+} and Pb^{2+} toward low binding energies was attributed to the decrease in iodine vacancies owing to $TFSI^-$. Simultaneously, the shift in the peak of I^- toward low binding energy may be associated with the binding of I^- with Li^+ ions that fill A-site vacancies or occupy interstitial sites. The introduction of LiTFSI considerably retards the oxidation of Sn^{2+}, as illustrated in Figure 3B. Following a 12-h exposure of the NBG films to ambient air, the control NBG film exhibits a peak of oxidized Sn^{4+}, whereas two distinct peaks of Sn^{2+} and Sn^{4+} are observed for the LiTFSI-treated NBG film. We attribute the retardation of NBG perovskite oxidation primarily to the accumulation of $TFSI^-$ ions on the perovskite surface, as illustrated in Tof-SIMS (Figure 3A). These $TFSI^-$ ions form a protective layer, believed to hinder oxygen from interacting with the perovskite surface and potentially raising the ionization potential.[48] Therefore, the improvement of the device stability caused by treatment with LiTFSI shown above was attributed to the increase in the resistance of the surface to oxidation owing to LiTFSI coverage. In addition, the decrease in I^- vacancies, which likely play a crucial role in degradation by facilitating iodide ion migration to reactive surfaces and favoring the generation of I_2/I_3^- species, is responsible for the improvement of the environmental stability of NBG perovskite.[49]

Some early studies have raised concerns about the impact of LiTFSI on device stability because it is known that LiTFSI absorbs moisture due to the hydrophilic nature of Li^+ ions,[50–52] and Li^+ ions can migrate toward the surface, accelerating the infiltration of moisture and oxygen.[44,51,53] For these reasons, LiTFSI potentially exacerbate device stability when the it is used as a p-dopant for the hole transporting layers (Spiro-OMeTAD) in n-i-p-type PSCs because hole transporting layer in an n-i-p-type device is typically exposed directly to air. However, in our study, a very thin LiTFSI layer is sandwiched between the perovskite and the upper multiple electron transporting layers. Therefore, the LiTFSI layer is protected from direct contact with air. Moreover, our devices were encapsulated using epoxy and cover glass, further shielding the samples from external factors. Additionally, our fabrication process involved processing LiTFSI in a high-purity Ar-filled glove box, where the concentration of oxygen and moisture was maintained below 0.1 ppm, thereby minimizing the likelihood of LiTFSI reacting with environmental elements.

Ultraviolet photoemission spectroscopy (UPS) measurements were performed to investigate the energy band structure modulation in NBG perovskites (Figure 3C). A schematic of energy levels derived from UPS spectra reveals that the Fermi level (E_F) of the LiTFSI-treated NBG film is situated 0.13 eV closer to the conduction band minimum than that of the control film (Figure 3D). The accumulation of $TFSI^-$ ions is believed to act as electron donors by releasing free electrons to the conduction band and inducing electron compensation for Sn^{4+}, thereby shifting the Fermi level closer to the conduction band. When the surface is more n-type character than the bulk of the film, band bending can be induced at the perovskite surface.[19,54] This promotes the well-constructed band alignment between the perovskite and the electron-transporting layer.[18]

For a better understanding of the underlying mechanism of LiTFSI influence on NBG perovskites, we have performed density functional theory (DFT) calculation as shown in Figure 3E. We investigated whether LiTFSI molecules were dissociated into Li and TFSI molecules and passivate the defective surface, especially iodine vacancies. Considering the experimental finding that Li^+ penetrates the bulk and $TFSI^-$ stays on the surface, Li^+ defects were placed at an interstitial site, and $TFSI^-$ was located around the iodine vacancy in the calculation. Since the iodine vacancy is a donor defect, we generated an iodine vacancy defect in the 1+ charged state at the surface by removing an iodine atom. As shown in the optimized structure (Figure 3E), the oxygen atoms of TFSI interact with the Sn atoms forming the vacancy. The binding energy of LiTFSI ($E_{tot}(\text{LiTFSI}) + E_{tot}(V_I^+) - E_{tot}(\text{LiTFSI} + V_I^+)$) is as large as 0.936 eV. This large binding energy indicates that LiTFSI can be dissociated into Li interstitial in the bulk perovskite and TFSI molecule passivating the iodine vacancy at the surface, which inhibits further degradation. Li interstitial is expected to mitigate the bulk defect density of NBG perovskites by inducing n-type doping and to suppress the migration of iodine by strongly interacting with perovskite lattice cage.[45–47] Comprehensively, we could think that LiTFSI reduces nonradiative charge recombination at the surface and in the bulk, while slows down the oxidation of NBG perovskite, enhancing the PV properties and stability of NBG PSCs.

2.4 | Performance of LiTFSI-treated all-perovskite tandem devices

We then fabricated monolithic all-perovskite tandem solar cells by combining control and LiTFSI-treated NBG bottom subcells with WBG top subcells (Figure 4A). As presented in Figure S9 and Table S3, our WBG PSC exhibits the highest PCE of 18.76% with a V_{OC} of 1.256 V, J_{SC} of 17.88 mA cm^{-2}, and FF of 83.52%. As shown in PCE histogram (Figure 4B), all-perovskite tandems with LiTFSI exhibit a higher average PCE (26.87 ± 0.40) than those without LiTFSI (25.93 ± 0.40). This enhancement

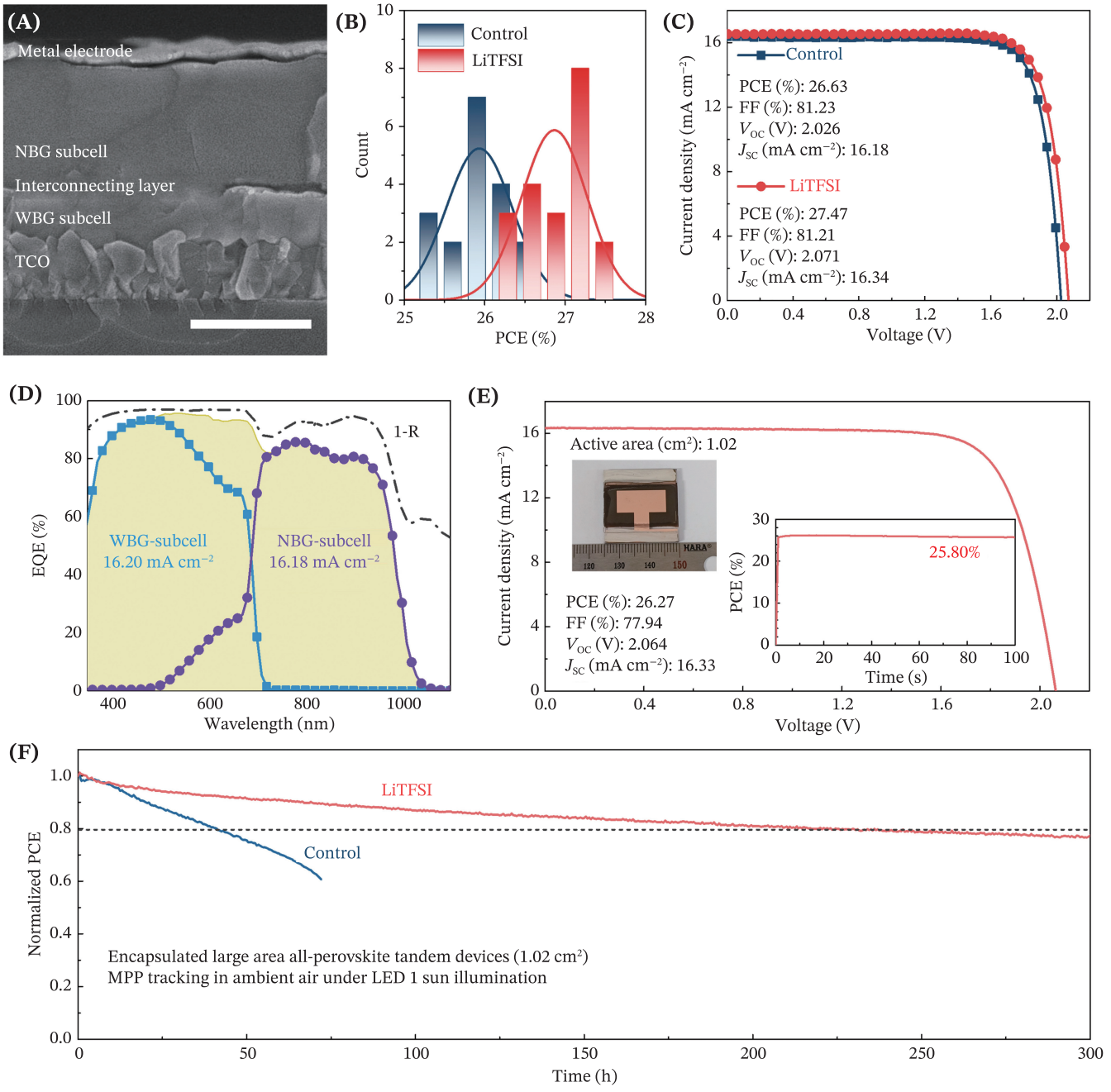

FIGURE 4 PV performance of all-perovskite tandem solar cells. (A) Cross-sectional scanning electron microscopy image of all-perovskite tandem solar cell. Scale bar: 1 μm. (B) Histogram for PCE of all-perovskite tandems with and without LiTFSI for NBG subcells. (C) *J*–*V* curves of the best-performing all-perovskite tandems. (D) EQE and total absorptance ($1 - R$, where R is total reflectance) curves of LiTFSI-treated all-perovskite tandem. (E) *J*–*V* curve of the best-performing large-area (1.02 cm^2) all-perovskite tandem with the LiTFSI-treated NBG subcell. The inset shows an image of the large-area device. Another inset shows the stabilized power output. (F) Continuous MPP tracking of the encapsulated large-area tandems for 300 h under 1 sun illumination in ambient air at a relative humidity of 30%–50%. No forced cooling system was used during storage and measurement, and the environmental temperature was maintained at ~22°C. The initial PCEs of control and LiTFSI-treated tandems were 23.97% (V_{OC} = 1.968 V, FF = 74.99%, and J_{SC} = 16.24 mA cm^{-2}) and 25.14% (V_{OC} = 2.045 V, FF = 76.98%, and J_{SC} = 15.97 mA cm^{-2}), respectively.

was primarily attributed to the increase in V_{OC} and FF resulting from the incorporation of LiTFSI, which is consistent with the results observed for the single-junction NBG devices (Figure S10 and Table S4).

Figure 4C presents the *J*–*V* curves and corresponding PV parameters of the best-performing tandem cells. The LiTFSI-treated all-perovskite tandem exhibits an outstanding PCE of 27.47%, along with a V_{OC} of 2.071 V, FF

of 81.23%, and J_{SC} of 16.34 mA cm^{-2}. Furthermore, the best-performing tandem with LiTFSI shows a high stabilized PCE (27.16%) than that without LiTFSI (26.30%; Figure S11). The improvement in PCE, particularly in FF and V_{OC}, for LiTFSI-treated tandems was attributed to the reduction in defects in NBG subcells by LiTFSI. This agrees with dark *J–V* curves of the tandem devices, indicating a low saturation current in the LiTFSI-treated tandems (Figure S12). The integrated J_{SC} values of WBG and NBG subcells obtained from EQE spectra of LiTFSI-treated tandems are 16.20 and 16.18 mA cm^{-2}, respectively, which is in good agreement with the J_{SC} values determined through *J–V* measurements (Figure 4D).

To assess the upscaling potential of LiTFSI treatment for tandem cells, we fabricated large-area devices using the same process as that for small cells. A photograph of our large-area device with an aperture area of 1.02 cm^2 is shown in the inset of Figure 4E. The best-performing large-area tandem with LiTFSI exhibits a higher PCE of 26.27% (V_{OC} = 2.064 V, FF = 77.94%, and J_{SC} = 16.33 mA cm^{-2}) with a stabilized PCE of 25.80% than control device exhibiting PCE of 23.97% (V_{OC} = 1.968 V, FF = 74.99%, and J_{SC} = 16.24 mA cm^{-2}) (Figure S13). Histograms of PV parameters for large-area tandems indicate that the introduction of LiTFSI does not pose considerable issues for upscaling up to 1.02 cm^2 (Figure S14). The lower V_{OC} and FF than those in small-area devices were attributed to perovskite layer inhomogeneity resulting from upscaling.[55] In addition, we conducted maximum power point (MPP) tracking of encapsulated large-area all-perovskite tandem solar cells, with and without LiTFSI, under 1 sun illumination in ambient air (Figure 4F). The LiTFSI-treated tandem exhibits promising operational stability and maintains 80% of its initial PCE after 240 h of operation. This stability considerably surpasses the tandem device without LiTFSI, which maintained 80% of its initial PCE for ~40 h. We attributed this enhanced stability to the suppression of defects at the surface and in the bulk and to the protection of the NBG surface from oxidation by LiTFSI. It is worth noting that initial rapid PCE loss (burn-in) observed in single-junction NBG devices does not appear in tandem devices. In a single-junction NBG device, hot carriers, generated when high-energy photons with energies significantly above the NBG perovskite are absorbed, dissipate their excess energy as heat.[56] Localized heating caused by the relaxation of hot carriers potentially accelerate degradation of NBG perovskite through non-radiative recombination, ionic migration, and/or interface destruction in NBG perovskite layers.[57–59] In contrast, the tandem configuration can mitigate this issue because the WBG subcell absorbs high-energy photons from the solar spectrum. This can reduce the photon flux reaching the NBG subcell, thereby minimizing thermalization losses and the associated localized heating effects.

3 | CONCLUSION

Herein, we demonstrated the effectiveness of LiTFSI in enhancing the performance and stability of NBG subcells and all-perovskite tandem solar cells. The LiTFSI bifunctionally passivated the defects at the surface and in the bulk, leading to reduced nonradiative recombination and improved charge lifetime and extraction. In addition, LiTFSI retarded the oxidation of NBG perovskites by covering and strongly interacting with the perovskite surface. Treatment with LiTFSI resulted in an improvement in FF and V_{OC} of single-junction NBG PSCs, resulting in an impressive PCE of 22.04% (certified PCE of 21.42%). This allowed us to achieve outstanding PCEs of 27.47% (0.0935 cm^2) and 26.27% (1.02 cm^2) for all-perovskite tandems. In addition to PCE, the continuous operation stability of large-area all-perovskite tandems was considerably improved, resulting in T_{80} of 240 h under 1 sun illumination in ambient air. Thus, the proposed approach is promising for fabricating efficient and stable all-perovskite tandem solar cells, thereby marking a considerable step in the development of next-generation PV technology.

4 | EXPERIMENTAL SECTION

4.1 | Materials

All the chemicals and solvents were used as received without additional purification process. Dimethyl sulfoxide (DMSO, 99.8%), dimethylformamide (DMF, 99.8%), ethyl acetate (99.8%), isopropyl alcohol (IPA, 99.5%), chlorobenzene (CB, 99.8%), acetonitrile (99.8%), 4-tertbutylpyridine (96%), ethylenediamine (EDA, 99%), CsI (99.99%), SnF_2 (99%), Sn metal powder (99%), lead(II) thiocyanate ($Pb(SCN)_2$, 99.5%), Ethane-1,2-diammonium iodide ($EDAI_2$, 98%), and BCP (99%) were purchased from Sigma-Aldrich. FAI (99.99%), MAI (99.99%), MABr (99.99%), MACl (99.99%), and cobalt (III) TFSI were purchased from Greatcell Solar. [2-(9H-Carbazol-9-yl)ethyl]phosphonic acid (2PACz, >98%), $PbBr_2$ (99.99%), and PbI_2 powder (99.99%) were purchased from Tokyo Chemical Industry Co (TCI, Japan). SnI_2 beads (99.999%), PbI_2 beads (99.999%), and LiTFSI (99%), SnO_2 colloidal solution (15% in H_2O colloidal dispersion) were purchased from Thermo Fisher Scientific. PEDOT:PSS (CLEVIOS P VP AI 4083) was purchased from Heraeus, LLC. C_{60} is purchased from One-materials. 2,2,7,7-Tetrakis(*N*,*N*-di-p-methoxyphenylamine)-9,9-spirobifluorene (Spiro-OMeTAD, 99.5%) was purchased from Luminescence Technology Corporation. Tetrakis(dimethylamino) tin (IV) (99.9%) was purchased from EGChem Co., Ltd. Graphene oxide was

purchased from Graphene Supermarket. Cu and Au pellets (3 mm Dia) were obtained from iTASCO.

4.2 | Perovskite precursor solution

NBG perovskite precursor: The NBG precursor solution was prepared following the previous reports.[60] The precursor solution of 2.2 M was prepared by mixing FAI/MAI and SnI_2/PbI_2 in molar ratios of 0.7:0.3 and 0.5:0.5 in mixed solvents of DMF and DMSO in the volume ratio of 3:1. A nominal amount of CsI was added to form $(CsI)_{0.07}(FA_{0.7}MA_{0.3}Pb_{0.5}Sn_{0.5I3})_{0.93}$ composition. SnF_2 (10 mol% relative to SnI_2), $Pb(SCN)_2$ (0.5 mol% relative to perovskite), MACl (1.0 mol% relative to perovskite) and tin powder (5 mg mL^{-1}) was added to the precursor solution and stirred at room temperature for overnight. Before spin coating, the precursor solution was filter through a 0.2 μm polytetrafluoroethylene (PTFE) syringe filter.

WBG perovskite precursor: WBG perovskite solution was prepared following the typical double cation process. In brief, 1.15 M stock solution was prepared by mixing PbI_2, $PbBr_2$, FAI, and MABr in a mixture of DMF and DMSO (4:1) to form a $(FA_{0.6}MA_{0.4})Pb(I_{0.6}Br_{0.4})_3$ perovskite composition. Exactly 10% of excessive PbI_2 is added to all the precursor solutions. The precursor solution was thoroughly mixed overnight and filtered through 0.2 μm PTFE syringe filter before spin coating.

4.3 | Solar cell fabrication

Single-junction NBG perovskite devices: The pre-patterned FTO glass of 2.5 × 2.5 cm^2 was used as substrate for the full device fabrication. The substrates were sequentially cleaned by sonication with detergent (Hellmanex solution), acetone, deionized water, and IPA, each for 3 min. Next, the FTO glass substrates were dried using nitrogen stream. Afterwards, the surface of FTO was treated with an UV-ozone for 20 min. PEDOT:PSS was spin-coated on UVO-treated FTO substrates at 5000 rpm for 30 s and annealed at 120°C for 30 min in ambient air. Samples were transferred to argon-filled glove box after cooling them down. A total of 100 μL of NBG perovskite precursor solution was dropped on the PEDOT:PSS coated substrates and spun at 4000 rpm for 40 s. Exactly 200 μL of ethyl acetate as anti-solvent was dropped on the spinning substrate at 10 s before the end of spin coating. The substrates were then annealed at 100°C for 10 min. $EDAI_2$ solution prepared by dissolving 0.5 mg $EDAI_2$ powder in 1 mL IPA was spin coated at 3000 rpm for 30 s and then annealed at 100°C for 3 min.[18] For the LiTFSI treatment, 0.1 mM LiTFSI solution dissolving LiTFSI powder in IPA was spin coated at 3000 rpm for 30 s and then annealed at 65°C for 3 min. After cooling, the substrates were transferred to the evaporation chamber for 20 nm C_{60}, 5 nm BCP, and 100 nm Cu deposition. Finally, devices were encapsulated with UV epoxy and cover glass for characterization.

Single-junction WBG perovskite devices: FTO glass substrates were transferred to the glove box after UV-ozone treatment. 2PACz solution (1 mM) prepared by dissolving 2PACz powder in IPA was spin-coated onto the FTO substrate at 3000 rpm for 30 s and then substrates were subsequently annealed at 100°C for 10 min. A total of 100 μL of WBG perovskite solution was spin-coated onto the glass/ITO/2PACz/ at 6000 rpm for 30 s. Exactly 200 μL of CB was dripped onto the center of film at 25 sec before the end of spin coating. As-coated perovskite films were then annealed on hotplate at 100°C for 20 min. After perovskite annealing, 100 μL of EDA solution (0.1 mM EDA in toluene) was spin-coated onto perovskite at a speed of 3000 rpm for 30 s and then annealed on hotplate at 65°C for 5 min. After cooling, the substrates were transferred to the evaporation chamber for 20 nm C_{60}, 5 nm BCP, and 100 nm Cu deposition.

All-perovskite tandem devices: After the deposition of C_{60} on the top of WBG perovskite layer, samples were taken out and transferred to atomic layer deposition system (CN1, Atomic-Classic). A total of 25 nm SnO_2 was deposited using tetrakis(dimethylamino) tin (IV) precursor and deionized water at 90°C. Afterward, graphene oxide was deposited on the SnO_2 layer in ambient atmosphere. After then, the processes were identical to the single-junction NBG device. Large area devices with the active area of 1.02 cm^2 were fabricated using the same methods as small area devices. Only difference was that the active area (metal contact area) and illuminated aperture area.

4.4 | Solar cell characterization

Device characterizations were carried out under ambient air conditions after encapsulating the devices. *J–V* characteristics were measured using a source meter (Keithley 2450, Keithley), from forward bias to reverse bias, at a scan rate of 100 mV s^{-1}. a solar simulator (Oriel Solar 3A Class, 94023A, Newport), which was calibrated to illuminate AM 1.5G (100 mW cm^{-2}) using a standard Si reference cell (91150V, Newport), was utilized. The device contact area, that is, the overlapped area between the bottom and top electrode, was 0.16 cm^2 (1.2375 cm^2) and the illuminated active area of the device was 0.0935 cm^2 (1.02 cm^2) for small (large) area devices. The steady-state

PCEs were measured using a potentiostat (PGSTAT204, Autolab). Dark *J–V* curves and *I–V* traces were measured using a source meter (Keithley 4200-SCS, Keithley). Device configurations for space charge–limited current analysis were glass/ITO/SnO_2/PVSK/C_{60}/Cu and glass/ITO/PEDOT:PSS/PVSK/Spiro-OMeTAD/Au for electron- and hole-only devices, respectively. The electron- and hole-only device preparation were prepared following previous report.[61] EQE spectra of single-junction NBG devices were measured using a tunable light source for QE (TLS-300XU, Newport).

The EQE measurements for all-perovskite tandem solar cells were conducted using a Newport-Oriel IQE200 equipped with a 100 W Xenon lamp. The measurements were conducted in ambient air with a chopper set at a frequency of 29.0 Hz. The bias illumination for the WBG subcell was provided by an NIR LED illuminator with an emission peak at 850 nm, while for the NBG subcell, a blue LED illuminator with an emission peak at 460 nm was used. MPP tracking was performed with a Keithley 2400 source meter. It was conducted in ambient air with relative humidity of 30%–50%. No forced cooling system was used during storage and measurement, and the environmental temperature was maintained at ~22°C. One Sun simulated by the LED solar simulator (LSH-7320, Newport) was used as a light source. Mott–Schottky measurement was performed using the potentiostat (PGSTAT204, Autolab). Light-intensity dependent V_{OC} measurement was performed using the source meter (Keithley 2450, Keithley) and the LED solar simulator (LSH-7320, Newport). Light intensity was varied from 9.5 to 124.4 mW cm^{-2}. Each intensity was confirmed using the standard Si reference cell (91150V, Newport).

4.5 | Other characterizations

The surface morphology and cross-sectional images were observed via a field-emission scanning electron microscope (FE-SEM, JSM-6701F, JEOL). Absorption and reflectance spectra of the perovskite thin films were obtained via UV–vis–NIR spectroscopy (Cary 5000, Agilent Technologies). Integrating sphere was used to obtain the reflectance spectrum. ToF-SIMS measurement was carried out using an M6 Hybrid SIMS (ION-TOF GmbH, Münster, Germany) installed at the KBSI Busan Center. Samples were in negative and positive mode using an argon sputter gun at 5 keV (2.5 nA) and a Bi^{3+} analysis gun at 0.6 pA. Steady-state PL spectra were measured by dividing and guiding emission photons through an optical fiber to the external spectrometer (F-7000, Hitachi). TRPL study was carried out using a confocal microscope (MicroTime-200, Picoquant, Germany) with a 10× (air) objective. The lifetime measurements were performed at the Korea Basic Science Institute (KBSI), Daegu Center, Korea. A single-mode pulsed diode laser (470 nm with a pulse width of ~30 ps and an average power of ~1 μW operating in 500 kHz repetition rate) was used as an excitation source. A dichroic mirror (490 DCXR, AHF), a long-pass filter (HQ500lp, AHF), a 150 μm pinhole, a longpass filter (FEL0800 nm, Thorlabs), and a single photon avalanche diode (PDM series, MPD) were used to collect emission from the samples. A time-correlated single-photon counting system (PicoHarp-300, PicoQuant GmbH, Germany) was used to count emission photons. PL lifetime images consisting of 200 × 200 pixels were recorded using the time-tagged time-resolved (TTTR) data acquisition method. Exponential function fittings for the obtained PL decays were performed using Symphotime-64 software (Ver. 2.2). The surface chemical states of the PVSK films were analyzed via x-ray photoelectron spectroscopy (XPS, Theta Probe AR-XPS System, Thermo Fischer Scientific). The work function and valence band maximum (VBM) of the PVSK film were obtained using ultraviolet photoelectron spectroscopy (UPS, AXIS NoVA, Kratos) with a He–I line lamp (21.2 eV).

4.6 | DFT calculation

We performed density functional theory calculation using the projector augmented wave method,[62] as implemented in the Vienna Ab Initio Simulation Package.[63] The exchange-correlation functional parametrized by Perdew, Burke, and Erzernhof was used.[64] We employed Grimme's D3 method with the Becke–Johnson damping function for a better description of the dispersion interaction.[65] The plane waves were expanded up to 400 eV, and the structures were optimized until the residual forces became less than 0.03 eV $Å^{-1}$. To simulate the molecule adsorption, we employed a slab geometry in which the two layers are kept fixed to maintain the bulk-like region. A supercell was generated by expanding the cells three times each along the surface in parallel directions. The molecules were adsorbed on the fully relaxed side.

ACKNOWLEDGMENTS

This work was supported by the National Research Foundation of Korea (NRF, 2022M3J1A1085285, RS-2023-00302646, and 2022M3H4A1A03074093) funded by the Ministry of Science and ICT (MSIT).

CONFLICT OF INTEREST STATEMENT

The authors declare no conflict of interest.

DATA AVAILABILITY STATEMENT

The data that support the findings of this study are available in the supplementary material of this article.

ORCID

Ji-Sang Park https://orcid.org/0000-0002-1374-8793
Sangwook Lee https://orcid.org/0000-0002-3535-0241

REFERENCES

1. Tong JH, Song ZN, Kim DH, et al. Carrier lifetimes of >1 μs in Sn-Pb perovskites enable efficient all-perovskite tandem solar cells. *Science*. 2019;364(6439):475-479.
2. Lin RX, Xiao K, Qin ZY, et al. Monolithic all-perovskite tandem solar cells with 24.8% efficiency exploiting comproportionation to suppress Sn(II) oxidation in precursor ink. *Nat Energy*. 2019;4(10):864-873.
3. Li CW, Song ZN, Chen C, et al. Low-bandgap mixed tin-lead iodide perovskites with reduced methylammonium for simultaneous enhancement of solar cell efficiency and stability. *Nat Energy*. 2020;5(10):768-776.
4. Xiao K, Lin RX, Han QL, et al. All-perovskite tandem solar cells with 24.2% certified efficiency and area over 1 cm^2 using surface-anchoring zwitterionic antioxidant. *Nat Energy*. 2020;5(11):870-880.
5. Wu X, Xiong GQ, Yue ZY, Dong ZY, Cheng YH. Defect passivation engineering of wide-bandgap perovskites for high-performance solar cells. *Mater Chem Front*. 2024;8(3):800-813.
6. Leijtens T, Bush KA, Prasanna R, MD MG. Opportunities and challenges for tandem solar cells using metal halide perovskite semiconductors. *Nat Energy*. 2018;3(10):828-838.
7. Lin R, Wang Y, Lu Q, et al. All-perovskite tandem solar cells with 3D/3D bilayer perovskite heterojunction. *Nature*. 2023;620(7976):994-1000.
8. NREL. Best research-cell efficiencies 2024. https://www.nrel.gov/pv/assets/pdfs/best-research-cell-efficiencies.pdf
9. Li LD, Wang YR, Wang XY, et al. Flexible all-perovskite tandem solar cells approaching 25% efficiency with molecule-bridged hole-selective contact. *Nat Energy*. 2022;7(8):708-717.
10. Lang FL, Chiang YH, Frohna K, et al. Methylammonium-free co-evaporated perovskite absorbers with high radiation and UV tolerance: an option for in-space manufacturing of space-PV? *RSC Adv*. 2023;13(31):21138-21145.
11. Chen L, Li CW, Xian YM, et al. Incorporating potassium citrate to improve the performance of tin-lead perovskite solar cells. *Adv Energy Mater*. 2023;13(32):2301218.
12. Zhou S, Fu S, Wang C, et al. Aspartate all-in-one doping strategy enables efficient all-perovskite tandems. *Nature*. 2023;624(7990):69-73.
13. Zhao D, Chen C, Wang C, et al. Efficient two-terminal all-perovskite tandem solar cells enabled by high-quality low-bandgap absorber layers. *Nat Energy*. 2018;3(12):1093-1100.
14. Gunasekaran RK, Jung JA, Yang SW, et al. High-throughput compositional mapping of triple-cation tin-lead perovskites for high-efficiency solar cells. *Infomat*. 2023;5(4):e12393.
15. Tong JH, Jiang Q, Ferguson AJ, et al. Carrier control in Sn-Pb perovskites via 2D cation engineering for all-perovskite tandem solar cells with improved efficiency and stability. *Nat Energy*. 2022;7(7):642-651.
16. Yang FJ, MacQueen RW, Menzel D, et al. Rubidium iodide reduces recombination losses in methylammonium-free tin-lead perovskite solar cells. *Adv Energy Mater*. 2023;13(19):2204339.
17. Gunasekaran RK, Jung J, Yang SW, et al. Regulating surface heterogeneity maximizes photovoltage and operational stability in tin-lead perovskite solar cells. *ACS Energy Lett*. 2023;9(1):102-109.
18. Hu SF, Otsuka K, Murdey R, et al. Optimized carrier extraction at interfaces for 23.6% efficient tin-lead perovskite solar cells. *Energ Environ Sci*. 2022;15(5):2096-2107.
19. Liang Z, Xu HF, Zhang Y, et al. A selective targeting anchor strategy affords efficient and stable ideal-bandgap perovskite solar cells. *Adv Mater*. 2022;34(18):2110241.
20. Wei MY, Xiao K, Walters G, et al. Combining efficiency and stability in mixed tin-lead perovskite solar cells by capping grains with an ultrathin 2D layer. *Adv Mater*. 2020;32(12):1907058.
21. Zhang L, Kang Q, Shi HX, et al. Surface defect passivation of Pb-Sn-alloyed perovskite film by 1,3-propanediammonium iodide toward high-performance photovoltaic devices. *Solar RRL*. 2021;5(8):2100299.
22. Lin RX, Xu J, Wei MY, et al. All-perovskite tandem solar cells with improved grain surface passivation. *Nature*. 2022;603(7899):73-78.
23. Chen H, Maxwell A, Li CW, et al. Regulating surface potential maximizes voltage in all-perovskite tandems. *Nature*. 2023;613(7945):676-681.
24. Liu XX, Zhang ZF, Lin F, Cheng YH. Structural modulation and assembling of metal halide perovskites for solar cells and light-emitting diodes. *Inf Dent*. 2021;3(11):1218-1250.
25. Yang T, Ma C, Cai W, et al. Amidino-based Dion-Jacobson 2D perovskite for efficient and stable 2D/3D heterostructure perovskite solar cells. *Joule*. 2023;7(3):574-586.
26. Mathew P, Cho J, Kamat PV. Ramifications of ion migration in 2D lead halide perovskites. *ACS Energy Lett*. 2024;9(3):1103-1114.
27. Zhong Y, Yang J, Wang XY, et al. Inhibition of ion migration for highly efficient and stable perovskite solar cells. *Adv Mater*. 2023;35(52):e2302552.
28. Liu X, Zheng BL, Shi L, et al. Perovskite solar cells based on spiro-OMeTAD stabilized with an alkylthiol additive. *Nat Photonics*. 2023;17(1):96-105.
29. Zhang TK, Wang F, Kim HB, et al. Ion-modulated radical doping of spiro-OMeTAD for more efficient and stable perovskite solar cells. *Science*. 2022;377(6605):495-501.
30. Nakka L, Cheng Y, Aberle AG, Lin F. Analytical review of Spiro-OMeTAD hole transport materials: paths toward stable and efficient perovskite solar cells. *Adv Energy Sustain Res*. 2022;3(8):2200045.
31. Yu Z, Wang J, Chen B, et al. Solution-processed ternary tin (II) alloy as hole-transport layer of Sn–Pb perovskite solar cells for enhanced efficiency and stability. *Adv Mater*. 2022;34(49):2205769.
32. Tan S, Yavuz I, Weber MH, et al. Shallow iodine defects accelerate the degradation of α-phase formamidinium perovskite. *Joule*. 2020;4(11):2426-2442.
33. Domanski K, Roose B, Matsui T, et al. Migration of cations induces reversible performance losses over day/night cycling in perovskite solar cells. *Energ Environ Sci*. 2017;10(2):604-613.

34. Domanski K, Alharbi EA, Hagfeldt A, Grätzel M, Tress W. Systematic investigation of the impact of operation conditions on the degradation behaviour of perovskite solar cells. *Nat Energy*. 2018;3(1):61-67.
35. Oliver RDJ, Caprioglio P, Peña-Camargo F, et al. Understanding and suppressing non-radiative losses in methylammonium-free wide-bandgap perovskite solar cells. *Energ Environ Sci*. 2022;15(2):714-726.
36. Krogmeier B, Staub F, Grabowski D, Rau U, Kirchartz T. Quantitative analysis of the transient photoluminescence of $CH_3NH_3PbI_3/PC_{61}BM$ heterojunctions by numerical simulations. *Sustain Energy Fuels*. 2018;2(5):1027-1034.
37. Wetzelaer G, Scheepers M, Sempere AM, et al. Trap-assisted non-radiative recombination in organic-inorganic perovskite solar cells. *Adv Mater*. 2015;27(11):1837-1841.
38. Tress W, Yavari M, Domanski K, et al. Interpretation and evolution of open-circuit voltage, recombination, ideality factor and subgap defect states during reversible light-soaking and irreversible degradation of perovskite solar cells. *Energy Environ Sci*. 2018;11(3):715.
39. Caprioglio P, Wolff CM, Sandberg OJ, et al. On the origin of the ideality factor in perovskite solar cells. *Adv Energy Mater*. 2020;10(27):2000502.
40. Stolterfoht M, Grischek M, Caprioglio P, et al. How to quantify the efficiency potential of neat perovskite films: perovskite semiconductors with an implied efficiency exceeding 28%. *Adv Mater*. 2020;32(17):2000080.
41. Al-Ashouri A, Köhnen E, Li B, et al. Monolithic perovskite/silicon tandem solar cell with >29% efficiency by enhanced hole extraction. *Science*. 2020;370(6522):1300-1309.
42. Xia JX, Zhang Y, Xiao CX, et al. Tailoring electric dipole of hole-transporting material p-dopants for perovskite solar cells. *Joule*. 2022;6(7):1689-1709.
43. Yun AJ, Kim J, Gil B, et al. Incorporation of lithium fluoride restraining thermal degradation and photodegradation of organometal halide perovskite solar cells. *ACS Appl Mater Interfaces*. 2020;12(45):50418-50425.
44. Li Z, Xiao CX, Yang Y, et al. Extrinsic ion migration in perovskite solar cells. *Energ Environ Sci*. 2017;10(5):1234-1242.
45. Tabi GD, Pham HT, Zhan H, et al. LiI doping of mixed-cation mixed-halide perovskite solar cells: defect passivation, controlled crystallization and transient ionic response. *Mater Today Phys*. 2022;27:100822.
46. Cao J, Tao SX, Bobbert PA, Wong C-P, Zhao N. Interstitial occupancy by extrinsic alkali cations in perovskites and its impact on ion migration. *Adv Mater*. 2018;30(26):1707350.
47. Atourki L, Ouafi M, Makha M, et al. Impact of Li doping on the photophysical properties of perovskite absorber layer $FAPbI_3$. *J Alloys Compd*. 2021;850:156696.
48. Yu D, Pan M, Liu G, et al. Electron-withdrawing organic ligand for high-efficiency all-perovskite tandem solar cells. *Nat Energy*. 2024;9(3):298-307.
49. Hernandez LH, Lanzetta L, Jang S, et al. Factors limiting the operational stability of tin-lead perovskite solar cells. *ACS Energy Lett*. 2023;8(1):259-273.
50. Christians JA, Schulz P, Tinkham JS, et al. Tailored interfaces of unencapsulated perovskite solar cells for >1,000 hour operational stability. *Nat Energy*. 2018;3(1):68-74.
51. Guo X, Li J, Wang B, et al. Improving and stabilizing perovskite solar cells with incorporation of graphene in the Spiro-OMeTAD layer: suppressed Li ions migration and improved charge extraction. *ACS Appl Energy Mater*. 2020;3(1):970-976.
52. Lee I, Yun JH, Son HJ. Kim T-S accelerated degradation due to weakened adhesion from Li-TFSI additives in perovskite solar cells. *ACS Appl Mater Interfaces*. 2017;9(8):7029-7035.
53. Jiang L-L, Wang Z-K, Li M, Li CH, Fang PF, Liao LS. Flower-like MoS_2 nanocrystals: a powerful sorbent of Li+ in the Spiro-OMeTAD layer for highly efficient and stable perovskite solar cells. *J Mater Chem A*. 2019;7(8):3655-3663.
54. Tan S, Huang TY, Yavuz I, et al. Surface reconstruction of halide perovskites during post-treatment. *J Am Chem Soc*. 2021;143(18):6781-6786.
55. Rakocevic L, Mundt LE, Gehlhaar R, et al. Loss analysis in perovskite photovoltaic modules. *Solar RRL*. 2019;3(12):1900338.
56. Choudhury BD, Ibarra B, Cesano F, et al. The photon absorber and interconnecting layers in multijunction organic solar cell. *Solar Energy*. 2020;201(4):28-44.
57. Zheng DG, Kim DH. Degradation mechanisms of perovskite light-emitting diodes under electrical bias. *Nanophotonics*. 2023;12(3):451-476.
58. Zou YT, Wu T, Fu F, et al. Thermal-induced interface degradation in perovskite light-emitting diodes. *J Mater Chem C*. 2020;8(43):15079-15085.
59. Kung PK, Li MH, Lin CF, Chen PT. How temperature impacts material properties and photovoltaic performance of mixed-halide perovskite *via* light-induced ion migration. *J Mater Chem C*. 2024;12(29):11181-11191.
60. Vidyasagar D, Yun Y, Cho JY, et al. Surface-functionalized hole-selective monolayer for high efficiency single-junction wide-bandgap and monolithic tandem perovskite solar cells. *J Energy Chem*. 2024;88(28):317-326.
61. Yun Y, Han GS, Park GN, et al. A wide bandgap halide perovskite based self-powered blue photodetector with 84.9% of external quantum efficiency. *Adv Mater*. 2022;34(51):2206932.
62. Blöchl PE. Projector augmented-wave method. *Phys Rev B*. 1994;50(24):17953-17979.
63. Kresse G, Furthmüller J. Efficient iterative schemes for ab initio total-energy calculations using a plane-wave basis set. *Phys Rev B*. 1996;54(16):11169-11186.
64. Perdew JP, Burke K, Ernzerhof M. Generalized gradient approximation made simple. *Phys Rev Lett*. 1996;77(18):3865-3868.
65. Grimme S, Ehrlich S, Goerigk L. Effect of the damping function in dispersion corrected density functional theory. *J Comput Chem*. 2011;32(7):1456-1465.

SUPPORTING INFORMATION

Additional supporting information can be found online in the Supporting Information section at the end of this article.

How to cite this article: Yun Y, Vidyasagar D, Kim S, et al. Simultaneous passivation of surface and bulk defects in all-perovskite tandem solar cells using bifunctional lithium salts. *InfoMat*. 2025;7(4):e12656. doi:10.1002/inf2.12656